Proceedings of the
Annual Stability Conference
Structural Stability Research Council
San Antonio, Texas, March 21-24, 2017

Characterization of Cold-Formed Steel Member Dimensions and Geometric Imperfections Based on 3D Laser Scanning

Xi Zhao[1] and Benjamin W. Schafer[2]

Abstract

The objective of this paper is to demonstrate how detailed 3D laser scans of cold-formed steel members may be used to characterize cross-section dimensions, including complete information on the correlation between dimensions, as well as other manufacturing imperfections such as bow, camber, twist, crown, and flare. Advancing the use of simulation in design requires that manufacturing imperfections be understood, such that simulations are based on realistic geometry. This is particularly important for thin-walled members due to the well-known imperfection sensitivity of such members in certain failure mechanisms. C sections are selected for demonstration in this paper. The members are all scanned in a custom-built 3D laser scanner that results in a dense point cloud defining the true geometry of the outside surface of the scanned members. Algorithms are employed to post-process the point cloud into useful information including dimensions and geometric imperfections. The member dimensions (web height, flange length, corner radius, etc.) may be compared with nominally prescribed dimensions, and in addition the correlation across the dimensions is studied and the impact of typical manufacturing control is readily observed in the data. The imperfections (deviation from perfect) may be characterized in geometric terms: bow, camber, twist, crown of a given flat plate, flare of a given element; or may be characterized in terms of their modal buckling content: fit to flexural modes, torsional mode, local mode, and distortional mode. In addition, the geometric imperfections may be transformed into the frequency domain and power spectrum of the imperfection magnitudes can be obtained. This 1D spectrum approach provides a potentially novel means for generating realistic, but random geometric imperfections for use in shell finite element simulations. Shell finite element collapse analyses that compare the sensitivity in response to true, and various simulated imperfections are provided. The simulations indicate how simple modal imperfections are powerful for predicting strength conservatively, but the 1D spectral approach more closely approaches the results from the true (scanned) members. In the future larger Monte Carlo simulations should be performed to assess the reliability of cold-formed steel members using these results.

1. Background

Measurement Set-up

A full-field laser-based imperfection measurement platform has been built up in the Thin-Walled Structures Laboratory at Johns Hopkins University (Zhao et al. 2015). This imperfection

---

[1] Assistant Professor, West Virginia State University, <xi.zhao@wvstateu.edu>
[2] Professor, Johns Hopkins University, <schafer@jhu.edu>

measurement rig is made up of three major components, as shown in Fig. 1, and is capable to provide full-field geometric scanning on specimen within 10 inches (250 mm) in width and 8 feet (2400 mm) in length.

The laser scanner, a Keyence LJV-730 2D line laser, can generate 800 points per reading and measure a cross section up to 12 inches (304 mm) in width in the resolution of 0.01 inches (0.3 mm). The rotary stage can rotate the mounted laser scanner to any desired angle in the range of –140° to 140° so that any complex cross-section geometry can be measured. The linear drive system as the third major component can drive the rotary stage and laser scanner as commanded. The laser scanner is able to profile the target at high frequencies (up to 16 kHz), which allows it to scan and sample longitudinal measurements at command frequency. These three components cooperate and guarantee the function of this laser-based imperfection measurement platform to a lot of structural members, such as C, Z, and built-up C (BUC) sections placed on the support beam in the platform.

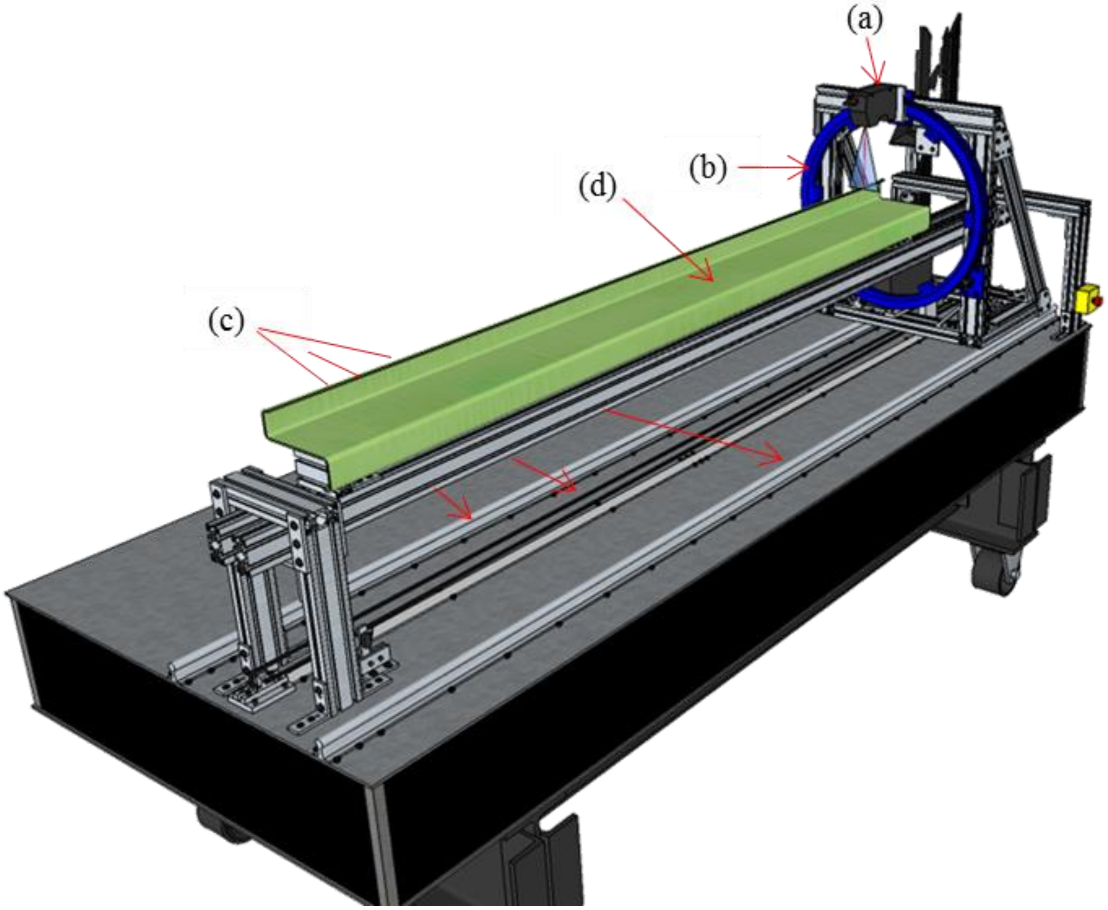

Figure 1 Full-field laser-based geometric imperfection measurement platform: (a) laser scanner; (b) rotary stage; (c) linear drive system; (d) targeted specimen. (Zhao et al. 2016).

Post-processing

The measurement point clouds are processed in four major steps before structural application. The first step is surface registration/construction. In this step, measured segments from several angles of view of the rotated laser are realigned and stitched together. An optimization algorithm called iterative closest points (ICP) has been used to estimate transformation values, i.e., translations in the cross-section plane and rotation about the longitudinal direction (Fig. 2). The second step is feature recognition, where points around a corner are fit to a constant corner feature (Fig. 3). A region that has maximum curvature and minimum fitting error is identified as a corner feature. The recognition method is executed on each cross section of measured segments. Thus, segments can be sorted into flat regions and curved regions.

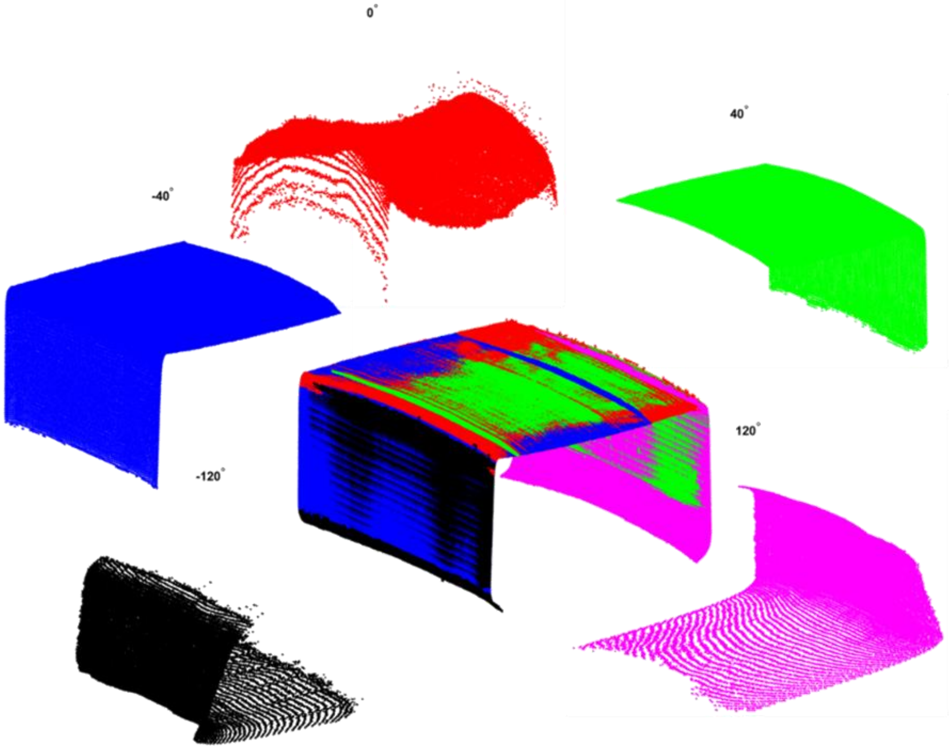

Figure 2 Surface registration of C section.

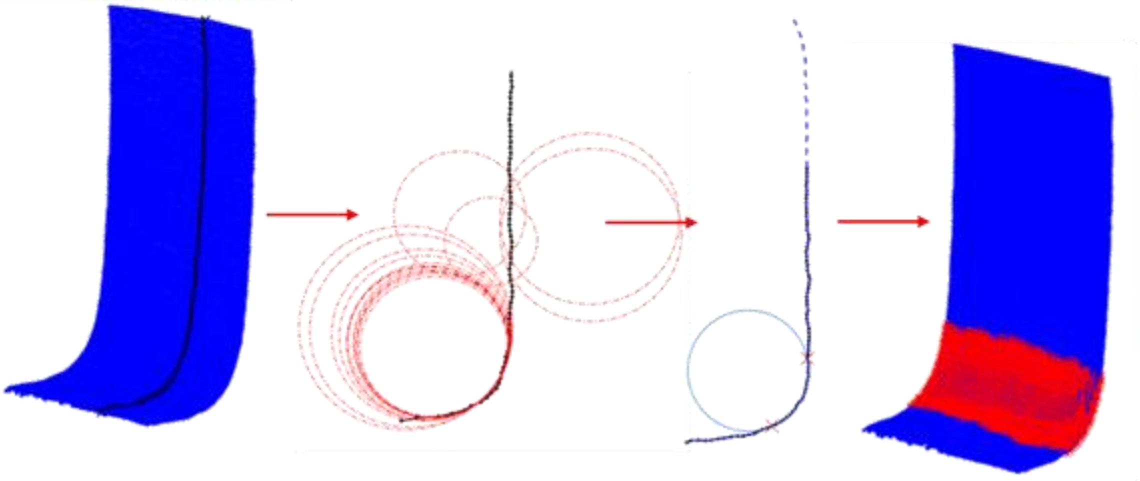

Figure 3 Procedures for corner feature recognition.

The third step is relatively simple, where the best resolution parts from measured segments are extracted to reconstruct the 3D model. The 3D models for C sections are displayed in Fig. 4, where the color map represents differences between true measured geometry and nominal shape.

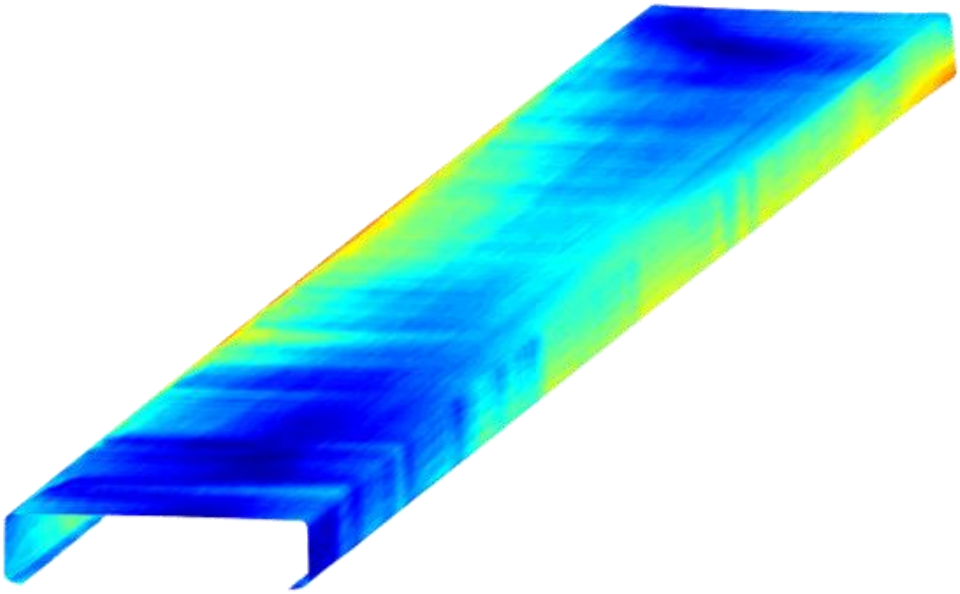

Figure 4 3D reconstructed models from laser measurements of C sections.

The reconstructed model generated from the above three steps can be directly applied to explore dimensions of the geometry cross-section by cross-section. Other applications such as imperfection characterization and finite element analysis (FEA) require one more post-processing step: point cloud downsampling and regularization. A perfect cross-section at a desired density is created as a reference with the aid from CUFSM (Li et al. 2011). Distances between the first node and following nodes are calculated as a reference to select operational points from the measurement point cloud. The procedure is repeated from one cross-section to the other until the end of the model. Prior to this step, a specific measurement filter has been applied to eliminate most of the measurement noises. More details can be referred to in Zhao et al. (2016).

2. Characterization of Dimensions

Definition of Dimensions of C

An important application from laser measurement point clouds is to calculate cross-section dimensions from reconstructed 3D models. Dimensions are not only statistically summarized as conventional but also studied in regards to its longitudinal variations as primary imperfections. Variation of dimensions leads to changes in section properties so as to create an impact on strength and stiffness of a structural member. Studies about the variations of dimensions have been rare due to the restriction of measurement tools where the laser-based measurement platform and its product (measurement point clouds) effectively fill the gap. Definitions of dimensions about the C sections are listed in Fig. 5. Radii are estimated from corners. Other regions are fitted with linear segments, intersections of which are used for calculating out-to-out dimensions.

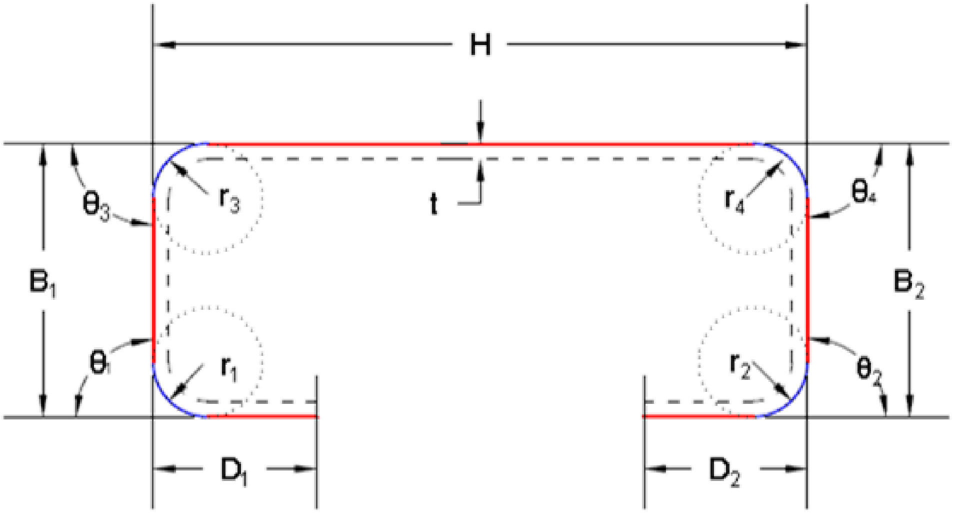

Figure 5 Dimension definitions of C.

Results of Dimensions

The study has been conducted with 28 C sections (14 Section 362S162-68 and 14 Section 600S137-54). More properties about these specimens can be referred to in Zhao (2016). Both C sections are 6 feet in length. Nominal dimensions of these specimens are shown in Table 1 (statistical dimension summaries of C sections).

Observed from the summary tables, corner radii far away from the web differ greatly from nominal dimensions. While corner radii adjacent to the web generally have better manufacturing control, deviations from the specified dimensions are much smaller in comparison with those close to the lip. Variation in the web depth has the best manufacturing control compared with all other dimensional quantities. The abundant data of dimension quantities enable the investigation of realizations of quality control standards as well as form the basis for fundamental reliability studies.

Table 1a Statistical summary from laser measurements of C sections (362S162-68)

Dimension		H (in)	B1 (in)	B2 (in)	D1 (in)	D2 (in)	R1 (in)	R2 (in)	R3 (in)	R4 (in)	θ1 (°)	θ2 (°)	θ3 (°)	θ4 (°)
Laser[a]	5%	3.71	1.58	1.68	0.52	0.45	0.30	0.26	0.32	0.29	74.4	85.5	90.9	91.9
	10%	3.71	1.59	1.69	0.52	0.46	0.31	0.26	0.33	0.30	74.7	85.8	91.1	92.2
	50%	3.72	1.60	1.70	0.54	0.48	0.32	0.27	0.35	0.34	75.6	87.2	91.6	93.0
	Mean	3.72	1.60	1.70	0.53	0.48	0.32	0.27	0.35	0.33	75.6	87.3	91.6	93.1
	Std	0.01	0.01	0.01	0.01	0.02	0.01	0.01	0.02	0.03	0.7	1.4	0.4	0.7
Nominal		3.63	1.63	1.63	0.50	0.50	0.18	0.18	0.18	0.18	90	90	90	90
L. vs. N. (%)[c]		2.6	-1.6	2.6	**6.9**	-3.6	**79.2**	**52.5**	**94.6**	**86**	**-16**	-3	1.7	3.4

a. Laser measurements from 548 cross sections x 14 specimens;
b. Thickness t was 0.0713inches (1.811 mm);
c. % Difference was established as |[mean (laser) – nominal]/[nominal]x100%

Table 1b Statistical summary from laser measurements of C sections (600S137-54)

Dimension		H	B_1	B_2	D_1	D_2	R_1	R_2	R_3	R_4	θ_1	θ_2	θ_3	θ_4
		(in)	(in)	(in)	(in)	(in)	(in)	(in)	(in)	(in)	(°)	(°)	(°)	(°)
Laser[a]	5%	5.99	1.29	1.26	0.37	0.37	0.17	0.17	0.12	0.13	77.6	76.4	86.3	87.5
	10%	6.00	1.30	1.27	0.38	0.37	0.17	0.17	0.12	0.13	78.4	76.7	87.1	87.7
	50%	6.01	1.32	1.28	0.40	0.39	0.18	0.18	0.13	0.14	80.4	77.7	87.7	88.1
	Mean	6.01	1.32	1.28	0.40	0.39	0.18	0.18	0.13	0.14	80.2	77.8	87.6	88.2
	Std	0.01	0.01	0.01	0.01	0.01	0.01	0.01	0.01	0.01	1.23	1.07	0.71	0.6
Nominal		6.00	1.38	1.38	0.38	0.38	0.14	0.14	0.14	0.14	90	90	90	90
L. vs. N. (%)[c]		0.1	-4.3	**-7.2**	**5.3**	2.6	**28.5**	**28.5**	-0.0	-0.0	**-11**	**-13**	-2.6	-2

a. Laser measurements from 548 cross sections x 14 specimens;

b. Thickness t was 0.0566 inches (1.437 mm);

c. % Difference was established as |[mean (laser) – nominal]/[nominal]x100%

Correlation study of C

Correlations among different dimensions deserve some attention because they can be used as the foundation for dimension-simulation studies. Fisher and Schafer (2016) used an assumed correlation matrix from variations of dimensions from the design values to generate large amounts of simulated dimensions, and the results were used to determine the impacts of strength and stiffness. Inspired by this idea, a correlation matrix with significance estimation (*p*-value) was produced from a Pearson linear correlation among variations of dimension quantities with respect to the C sections. Variations are from differences between measured dimensions and the mean of measured dimensions. Correlation matrices are displayed in Table 2, while the significance estimation tables are not listed in this paper due to the page limits. The significance values are generally satisfactory, and more details can be referred to in Zhao (2016).

Correlation studies have been done for C sections including 362S162-68 and 600S137-54. By combining the dimensional variations of both types of specimens, convincing correlation results can be obtained that follow traditional Pearson linear correlation theory, in which a correlation matrix can be formed for all 13 quantities. The matrix is symmetric, and data from the upper-right triangle of the matrix are enough for analysis. Values in the green grids are positive correlation factors, and values in the blue grids are negative correlation factors. B_1 is highly negative-correlated with B_2, and D_1 is highly negative-correlated with D_2. The findings from the correlation matrix verify the observations from the histograms of two types of C studs. In addition, B_1 shares a strong negative correlation with B_2, where the correlation factor is -0.65.

Table 2 Correlation Matrix of C

ρ	D_1	D_2	B_1	B_2	H	R_1	R_2	R_3	R_4	θ_1	θ_2	θ_3	θ_4
D_1	1.00	**-0.49**	0.27	**-0.40**	0.24	0.06	-0.11	-0.01	0.08	0.27	-0.27	0.25	0.15
D_2	-0.49	1.00	-0.20	0.18	-0.39	-0.05	0.22	-0.07	-0.29	-0.22	**0.42**	-0.37	**-0.46**
B_1	0.27	-0.20	1.00	**-0.65**	0.18	0.04	-0.01	0.13	0.13	**0.51**	-0.16	**0.45**	-0.02
B_2	-0.40	0.18	-0.65	1.00	0.03	-0.03	0.31	0.09	0.16	-0.30	0.34	-0.07	0.34
H	0.24	-0.39	0.18	0.03	1.00	0.00	-0.06	0.12	**0.62**	0.08	-0.31	0.29	**0.64**
R_1	0.06	-0.05	0.04	-0.03	0.00	1.00	0.20	0.09	0.29	0.05	0.11	0.06	0.05
R_2	-0.11	0.22	-0.01	0.31	-0.06	0.20	1.00	0.36	0.19	-0.09	**0.42**	0.05	-0.06
R_3	-0.01	-0.07	0.13	0.09	0.12	0.09	0.36	1.00	0.21	-0.15	0.16	0.09	-0.05
R_4	0.08	-0.29	0.13	0.16	0.62	0.29	0.19	0.21	1.00	0.16	-0.16	0.13	0.51
θ_1	0.27	-0.22	0.51	-0.30	0.08	0.05	-0.09	-0.15	0.16	1.00	**-0.52**	0.24	0.24
θ_2	-0.27	0.42	-0.16	0.34	-0.31	0.11	0.42	0.16	-0.16	-0.52	1.00	-0.05	-0.38
θ_3	0.25	-0.37	0.45	-0.07	0.29	0.06	0.05	0.09	0.13	0.24	-0.05	1.00	**0.46**
θ_4	0.15	-0.46	-0.02	0.34	0.64	0.05	-0.06	-0.05	0.51	0.24	-0.38	0.46	1.00

3. Characterization of Geometric Imperfections

Cold-formed steel members are sensitive to geometric imperfections due to their thin-walled property. Several researches have been carried out regarding geometric imperfections, especially for global imperfections. However, few researches have been executed for cross-section imperfections due to the minimal cross-section measurement data. Cross-section imperfection can be fulfilled via full geometry of the structural members obtained through the laser-based imperfection measurement platform.

Conventional Characterization of Geometric Imperfections

Past research characterizes geometric imperfections into five modes, i.e., bow, camber, twist, type 1, and type 2. Bow (G1), camber (G2), and twist (G3) belong to global imperfections; type 1 (d_1) and type 2 (d_2) belong to cross-section imperfections (Fig. 6).

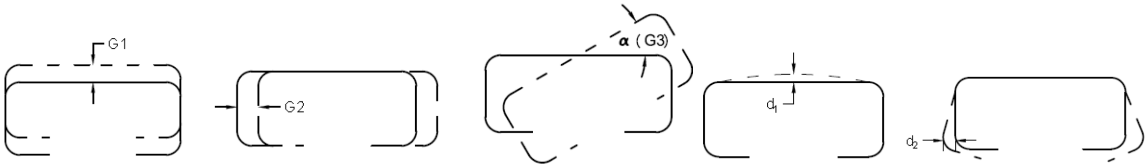

Figure 6 Conventional characterizations of geometric imperfections of C sections

The imperfection magnitudes are calculated from the reconstructed 3D point clouds from the laser-based imperfection measurement platform (Fig. 4). Details of the imperfection characterization method can be referred to in Zhao and Schafer (2016). Bow (G1) and camber (G2) imperfections are estimated from the centroid of a measured cross-section in comparison with the nominal cross-section centroids. The datum line is at the level of two ends of the measured sections. A mid-span cross-section is used to find the angle of twist of the entire specimen. The angle of twist is considered as the difference between the two ends. Regarding the cross-section imperfection, a type 1 imperfection is obtained by fitting a linear line to the ends of the web flat region and taking the maximum perpendicular deviation from the line; a type 2 imperfection is estimated from every cross-section by projecting an ideal flange vertical from the web flat and finding the perpendicular distance from the ideal flange to the actual flange again. Maximum values from each mode imperfection per specimen are considered as corresponding imperfection magnitudes, which are included for statistical summary.

The statistical summary with respect to C sections is listed in Table 3. Imperfections for all sections are obtained from over 7000 cross-section imperfections. Regarding C sections, twist imperfections of 362S162-68 and 600S137-54 are much smaller and generally stay within tolerance. However, they are still larger than in Zeinoddini's results. Type 1 of 362S162-68 contains a larger value when a 50% imperfection is compared with the tolerance and Zeinoddini's 50% results. Type 2 imperfections, however, approach to tolerance is c955 when a 50% imperfection is used.

Table 3 Statistical summary of geometric imperfection of C sections

C	362S162-68						600S137-54					
CDF	Type 1^a	Type 2^b		G1	G2	G3	Type 1^a	Type 2^b		G1	G2	G3
	d_1/t	d_{2L}/t	d_{2r}/t	L/δ	L/δ	°/ft	d_1/t	d_{2L}/t	d_{2r}/t	L/δ	L/δ	°/ft
25%	1.04	0.89	0.89	2988	2687	0.23	0.95	1.46	1.38	882	2422	0.07
50%	1.06	0.92	0.93	2271	2497	0.31	0.97	2.09	1.66	863	2239	0.09
75%	1.08	1.05	1.02	2162	2160	0.44	1.07	2.17	2.11	835	2024	0.11
95%	1.10	1.09	1.04	1969	1169	0.57	1.10	2.20	2.26	817	1543	0.14
99%	1.11	1.11	1.21	1969	1169	0.61	1.11	2.25	2.29	817	1543	0.15
mean	1.06	0.98	0.97	2547	2482	0.36	1.00	1.88	1.76	879	2394	0.09
Std. Dev.	0.03	0.09	0.10	458	646	0.15	0.08	0.39	0.42	70	577	0.03
Zeinoddini 50%^{c}	0.31	0.75	0.75	2909	4010	0.09	0.31	0.75	0.75	2909	4010	0.09
c955^d	0.92	0.92	0.92	960	960	0.99	1.15	1.15	1.15	960	960	0.60

b. Type 2 for conventional imperfections indicates over-bend or flare imperfections.

c. Measured values can be referred to in Zeinoddini (2011).

d. Reference tolerances from ASTM (2015) for C sections: G1 (bow) and G2 (camber) are L/960; G3 is 1/32 in./ft of a specimen, in addition for d1 (crown) = 1/16 in., and d2 (flare) = 1/16 in.

Modal Imperfection Decomposition of Geometric Imperfections

Characterization of imperfections are often connected to buckling modes to provide the longitudinal wavelength to supplement the in-plane magnitudes obtained from measurements. Conventional imperfection characterization sometimes may be too conservative with respect to cross-section imperfection. Modal imperfection decomposition (MID) characterizes imperfections based on first-mode buckling shapes across the buckling classes. Surface imperfections in a cross section are decoupled into five different modes, i.e., G1, G2, G3, distortional, and local where the deformation cross-section shapes are obtained from CUFSM analysis (Li et al. 2011). More details of these decomposition can be referred to (Zeinoddini 2011, Zhao et al. 2016).

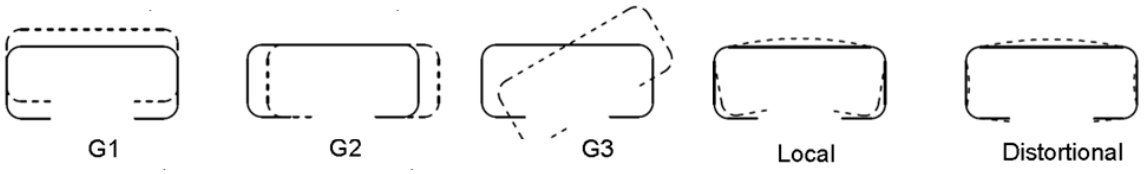

Figure 7 Modal imperfection decomposition of C.

As previously noted, for extreme values in a specimen, the conventional imperfections are an upper bound on the MID magnitudes for local and distortional and are essentially identical for global G1, G2, and G3. Results are shown in Table 4. Compared with Table 3, it is obvious that global imperfections between characterization methods are identical. However, the local and distortional modes' imperfections differ greatly compared with type 1 and type 2 imperfections. Section 362S162-68 shows 1.06 versus 0.58 between type 1 and local mode imperfection, 0.98 versus 0.43 between type 2 and distortional mode imperfection. Section 600S137-54 shows 1 versus 0.95 between type 1 and local mode imperfection, 1.88 versus 1.47 between type 2 and distortional mode imperfection. It can be observed that smaller sections may have more differences between the two characterization methods.

Table 4 Statistical summary of MID of C sections

C	362S162-68						600S137-54					
CDF	Local[a]	Distortional[b]		G1	G2	G3	Local[a]	Distortional[b]		G1	G2	G3
	d_{local}/t	$d_{dist.}/t$		L/δ	L/δ	°/ft	d_{local}/t	$d_{dist.}/t$		L/δ	L/δ	°/ft
25%	0.56	0.40		2988	2687	0.23	0.90	1.37		882	2422	0.07
50%	0.58	0.43		2271	2497	0.31	0.95	1.45		863	2239	0.09
75%	0.59	0.43		2162	2160	0.44	0.98	1.54		835	2024	0.11
95%	0.61	0.45		1969	1169	0.57	1.02	1.60		817	1543	0.14
99%	0.63	0.61		1969	1169	0.61	1.04	1.73		817	1543	0.15
mean	0.58	0.43		2547	2482	0.36	0.95	1.47		879	2394	0.09
Std. Dev.	0.03	0.06		458	646	0.15	0.05	0.12		70	577	0.03
Zeinoddini 50%[c]	0.31	0.75	0.75	2909	4010	0.09	0.31	0.75	0.75	2909	4010	0.09
c955[d]	0.92	0.92	0.92	960	960	0.99	1.15	1.15	1.15	960	960	0.60

a. Local imperfections for modal imperfections correlate to Type 1/crown imperfections.

b. Distortional imperfections for modal imperfections correlate to Type 2/ over-bend or flare imperfections.

c. Measured values can be referred to in Zeinoddini (2011).

d. Reference tolerances from ASTM (2015) for C sections: G1 (bow) and G2 (camber) are L/960; G3 is 1/32 in./ft of a specimen, in addition for d_1 (crown) = 1/16 in., and d_2 (flare) = 1/16 in., conventional C tolerances are reported here as similar tolerances for BUC as well as modal imperfections do not exist.

1D Spectral Method Based on MID

Characterization methods mentioned above are based on an assumption that a corresponding class of imperfections can relate to only one sinusoidal component longitudinally. For example, a global imperfection, bow (G1), may be represented by a half sinusoidal wave, the length and magnitudes of which are its overall length of the specimen and the statistical values of the maxima of the classified imperfections per specimen. This representation of imperfections may not be adequate for cross-section deviations and other global imperfections, such as camber and twist (Zeinoddin 2011). There should be a way that can correlate imperfections with multiple sinusoidal components along the length.

Inspired from this idea, 1D spectral representation of imperfection are introduced by Zeinoddini and Schafer (2012), method of which successfully have multiple sinusoidal components representing classified imperfections. Fourier transformation (Eq. 1) is employed to a specimen's imperfections characterized by modal imperfection decomposition (MID).

$$\alpha_i(y) \overset{FFT}{\leftrightarrow} \chi(f) \tag{1}$$

The magnitudes of Fourier-transformed imperfections are taken from their absolute values, while phase contents are not considered in this chapter. One pre-step is required before Fourier transformation is conducted, i.e., imperfections from measurements must be complemented with their asymmetry by considering that longitudinal imperfections use half sine-wave as their unit. Thus, the magnitudes of the Fourier transformations can be calculated as follows:

$$Mag(f) = \frac{|\chi(f)|}{N} \tag{2}$$

where N is the total number of points in the complete data from above step.

Based on the procedure mentioned above, imperfections in the frequency domain can be obtained for C sections (Figs. 8 and 9). It should be noted that the frequency axis (*x* axis) adopts reciprocals of half wavelengths as its representation. Section 362S162-68 (C) has extremely small magnitudes in the corresponding frequency in local imperfections (Fig. 8). Fifty percent of the imperfections from MID obtained magnitudes that were similar to those of 362S162-68, irrespective of frequency. However, Zeinoddini (2011) provided values that were about one-third of those of 362S162-68. Focusing on distortional spectrum plots, 50% MID again resembled the median of 365S162-68 (14 specimens) in magnitude. With respect to global imperfections, Zeinoddini's values coincided with the medians of the magnitudes and frequencies of the G1 and G2 imperfection spectra. But it was much smaller than the results of the traditional approaches as well as the actual 365S162-68 spectra.

Different situations occurred with 600S137-54 (C). The spectra of local and distortional imperfections shared their energy along multiple frequencies. Therefore, in general, the 50% MID values were larger than the maxima of the spectra. The magnitudes at the corresponding traditional frequencies of local and distortional imperfections were much more obvious than the spectra. Zeinoddini (2011) successfully predicted the spectra of distortional G2 and G3 imperfections, but it had smaller values in local and G1 imperfections.

It can be observed that nominally identical sections attain similar PSD curve shapes. This phenomenon creates a possibility to conclude mathematical representations for each type of specimen. The mathematical expressions can be found in Zhao et al. (2016).

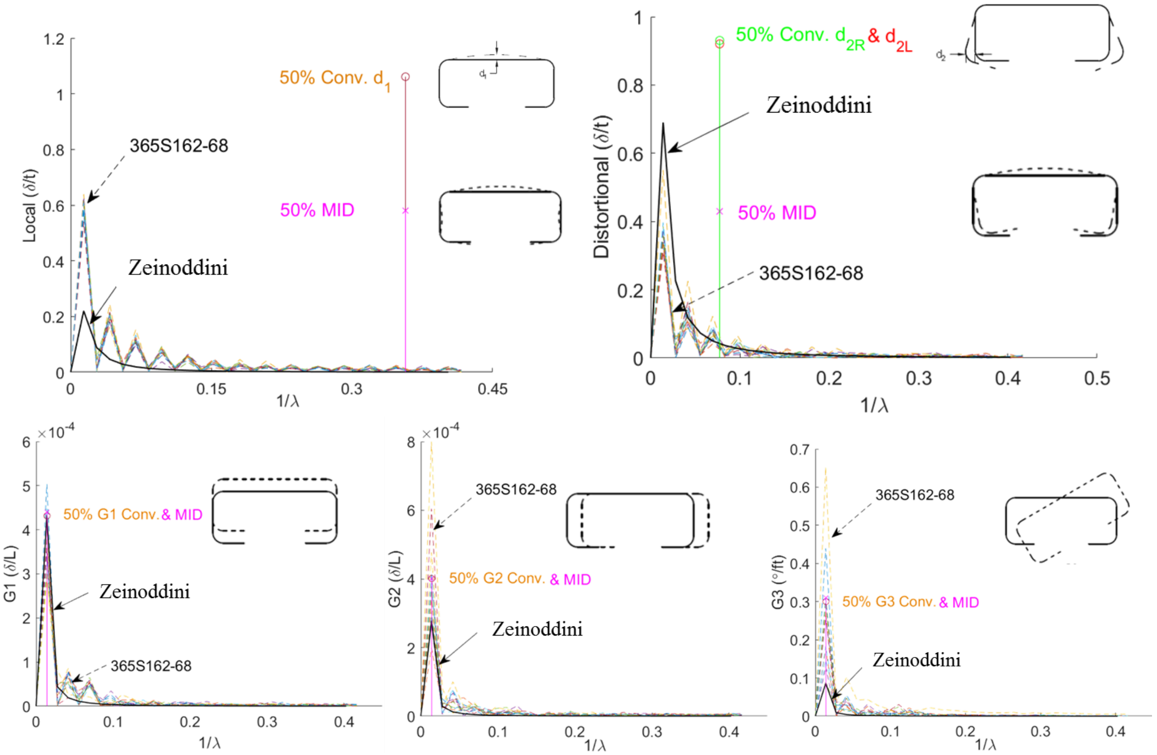

Figure 8 Comparisons among 1D spectral, design PSD, and traditional representation of C sections (362S162-68)

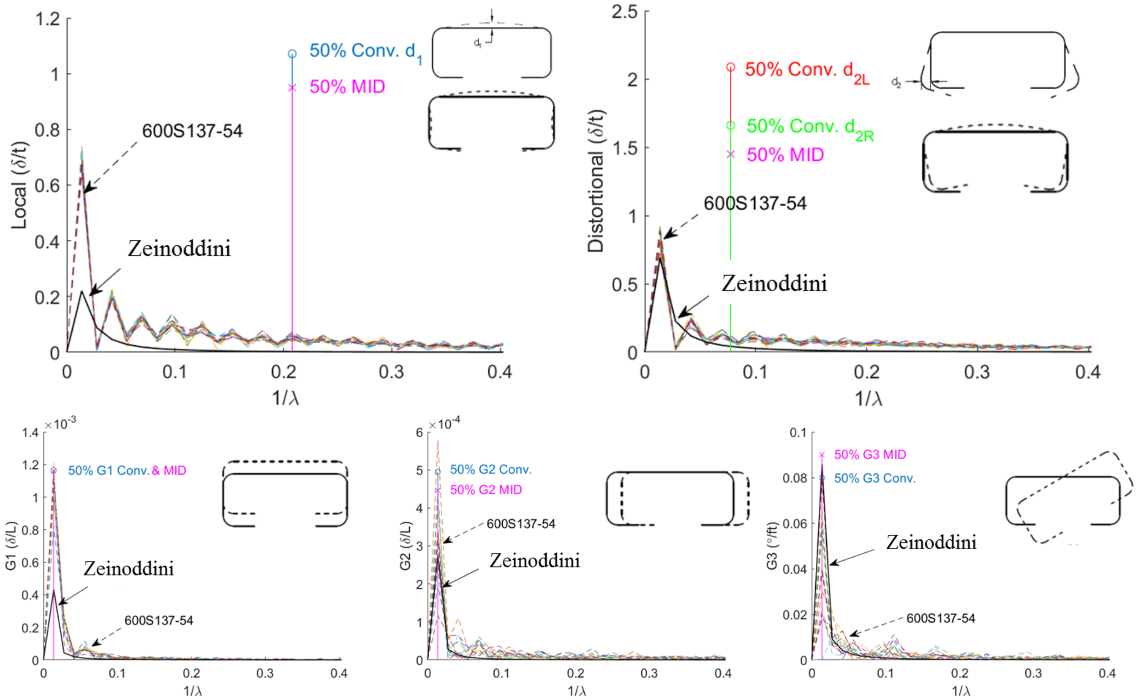

Figure 9 Comparisons among 1D spectral, design PSD, and traditional representation of C sections (600S137-54)

4. Simulation of Geometric Imperfection

True Geometric Imperfection Simulation

The post-processing steps provide access to application of point clouds to finite shell element modeling. Downsampling step in the post-processing can define desired elements across and along the sections. The point clouds (Fig. 10a), as a result of the fourth step in the post-processing, will be considered as nodes of finite element models. Nodes contain Cartesian coordinate information. Together with selected element type, S9R5, a model that can be directly imported to ABAQUS for finite element analysis is established, as shown in Fig. 10b. Thickness of shell-element models is determined from manual measurements. Materials properties are tested in the Thin-Walled Structural Laboratory (Fig. 11).

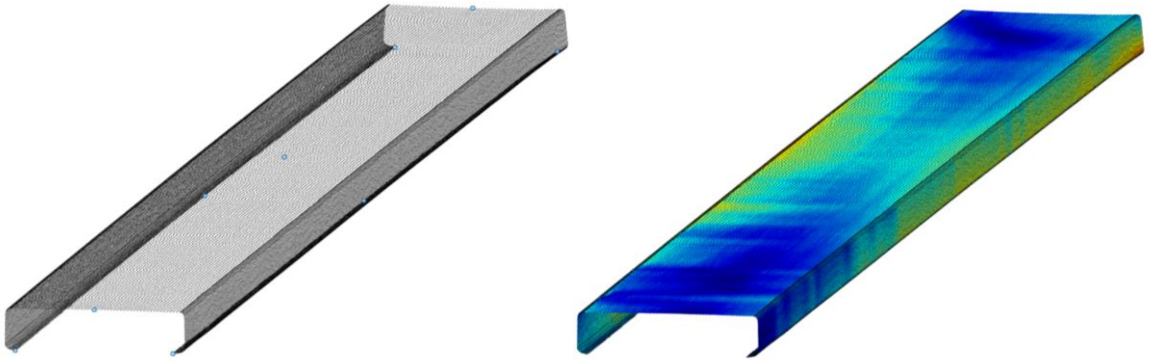

Figure 10 Models for Finite Element Analysis

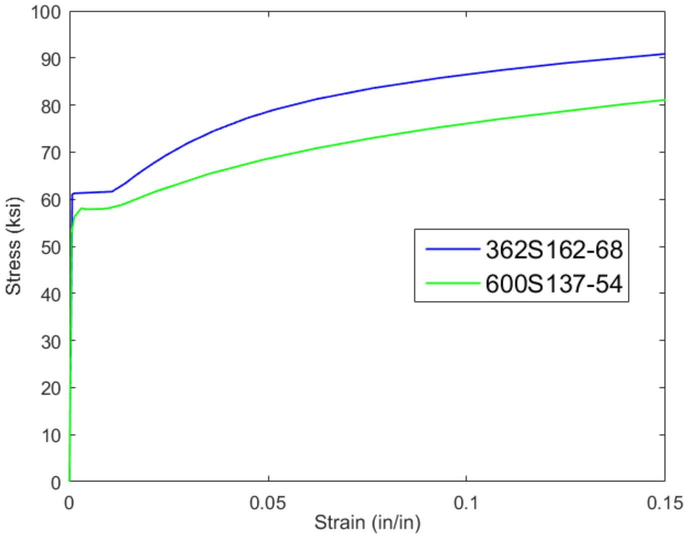

Figure 11 Material properties of modeled specimens

The following step is to determine the analysis method in the finite element analysis. Because a post-buckling analysis is required for cold-formed steel members, geometric nonlinearity and the material's nonlinearity must be considered. Three different methods can be used, i.e., the modified Riks method, the stabilize method, and the quasi-static method. The stabilize method is a bit tricky because an artificial damping coefficient is required, which generally must be estimated by trial and error. The quasi-static method treats collapse modeling in a slow, dynamic environment, where cold-formed steel analysis is rarely used, and abrupt changes occur in some models. Thus, the modified Riks method was chosen for use. For the purpose of comparison, arc-length definitions were fixed for a specific type of model (Table 5).

Table 5 Arc-length definitions using the modified Riks method

	Initial arc length	Total arc length	Minimum arc length	Maximum arc length
362S162-68	0.0001	1	1e-8	0.01
600s137-54	0.0001	1	1e-8	0.01

The final step is to determine the boundary conditions. Again, all models were assumed to be simply supported and warping fixed, where two reference nodes at both ends are defined to control end-plate nodes. One reference point was fixed in all three translation degrees of freedom. The other reference point was a defined displacement that the model should eventually reach.

All of the above information was integrated and used as input to the ABAQUS software, and a true geometry model was established, as shown in Fig. 12a. Thus, the six steps in the procedure described above were allowed to use point clouds of measured geometry to be analyzed in finite element approaches through the ABAQUS software. Figure 12b shows the result from collapse modeling analysis.

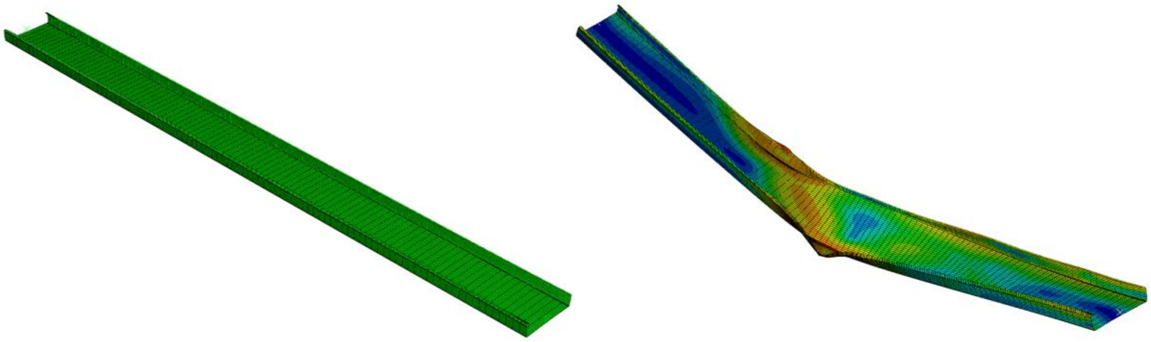

Figure 12 A finite element model of a true geometry in ABAQUS

Four true-geometry reconstructed models are chosen from each type of C sections, i.e., 362S162-68 and 600S137-54 (Fig. 13). It can be observed that load-displacement curves of both types of specimens are similar with minor differences in post-buckling stages as well as extrema. True geometry models with such similar ultimate loads and load-displacement curves are targeted as model justifications for numerical simulations of imperfection sensitivities.

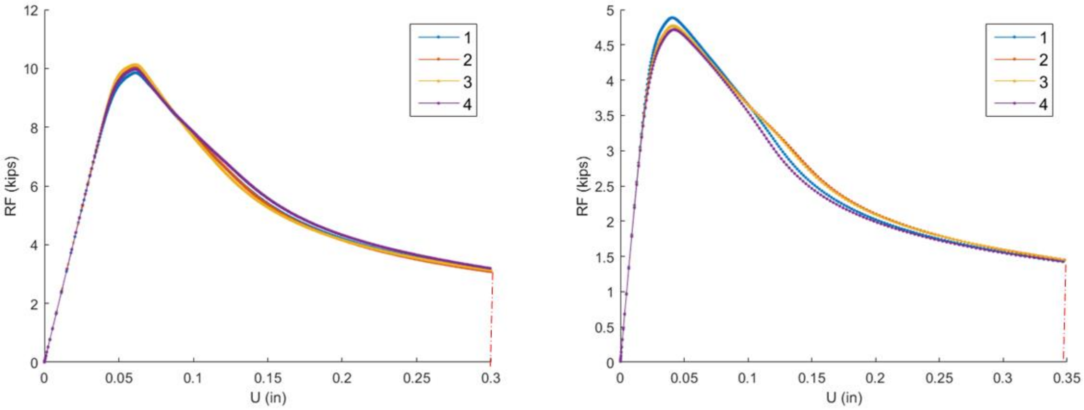

Figure 13 Load-displacement curves of collapse models: (a) 362S162-68; (b) 600S137-54.

Traditional Imperfection Simulation

To start the imperfection simulation, a model with nominal dimensions was established with nodes and elements ready. The imperfections were considered to add corresponding nodes to distort the model. Five modes of imperfections, i.e., local, distortional, bow, camber, and twists, were simulated, and cross-section deformation shapes were obtained from the corresponding buckling mode shape, as shown in Fig. 14. The deformation of a mode shape is normalized as a unit and then multiplied by the magnitudes of the imperfections from a statistical summary table. The results from these operations were added to the nodes of the model, thereby achieving the simulation of imperfection.

Regarding the preliminary study, the boundary conditions, arch length definitions, and material properties remain the same, as those described in *True Geometry Imperfection Simulation*.

Five characteristic imperfection modes were simulated in traditional representation, i.e., single sinusoidal components were assigned to corresponding imperfection modes. Different single mode imperfection modeling thoroughly demonstrates their impacts on failure modes and ultimate loads (Fig. 15 and Table 6). Conclusions from this preliminary study can be useful for further imperfection-combo simulations. The magnitudes of the imperfections were taken from the 50% CDF of statistical summaries of MID imperfections.

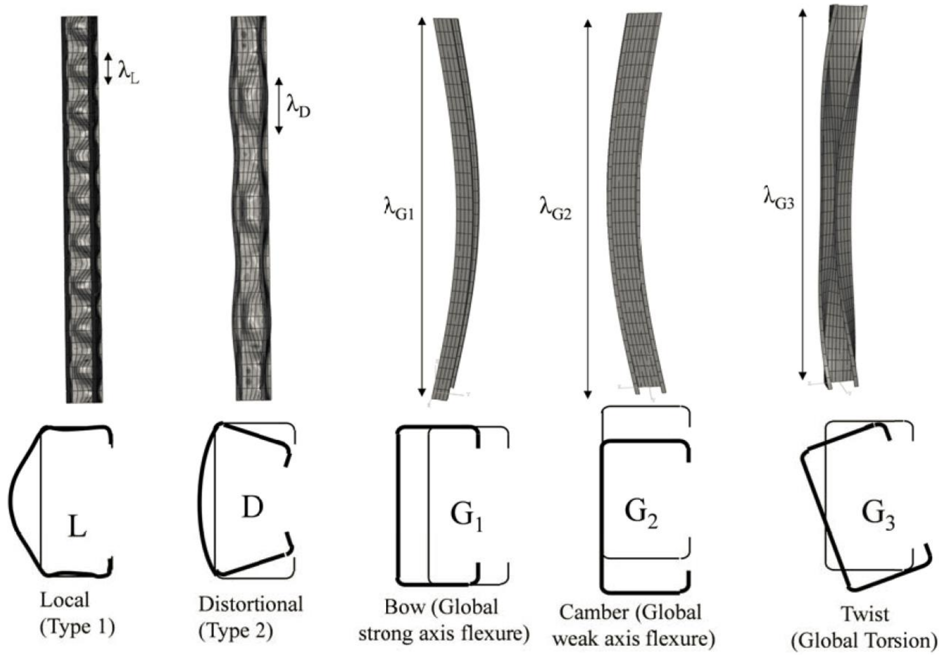

Figure 14 Imperfection simulations using traditional approach (Zeinoddini 2011)

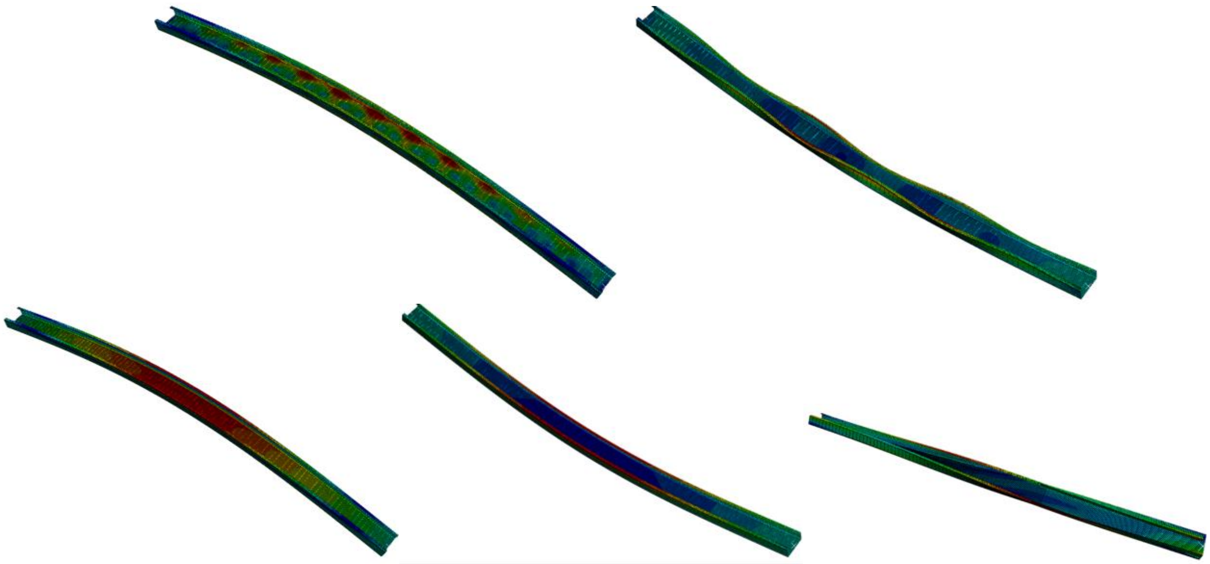

Figure 15 Typical Collapse modeling (600S137-54) of traditional approach: (a) Local; (b) Distortional; (c) Bow; (d) Camber; (e) Twist.

Table 6 Collapse Modeling Results of Traditional Approach

	Ultimate Load (kips)	
Imperfection mode	**362S162-68**	**600S137-54**
Local	7.67	4.06
Distortional	9.49	4.86
Bow	9.69	4.81
Camber	10.38	5.88
Twist	8.62	5.80

1D Spectral Imperfection Simulation

Collapse modeling using the 1D spectral approach is different from the traditional approach. Instead of assuming only one frequency for the corresponding imperfection mode, the classified mode imperfection in the 1D spectral approach is assumed to contain multiple frequencies. To begin the imperfection simulation, a series of base power spectra, with respect to local, distortional G1, G2, and G3, is obtained by estimating the medians of the power spectra from classified, measured imperfections (Fig. 16). The magnitudes of the first 10 frequencies are maintained for further analysis, the energy of which cannot be ignored because it occupies more than 95% of the classified imperfections.

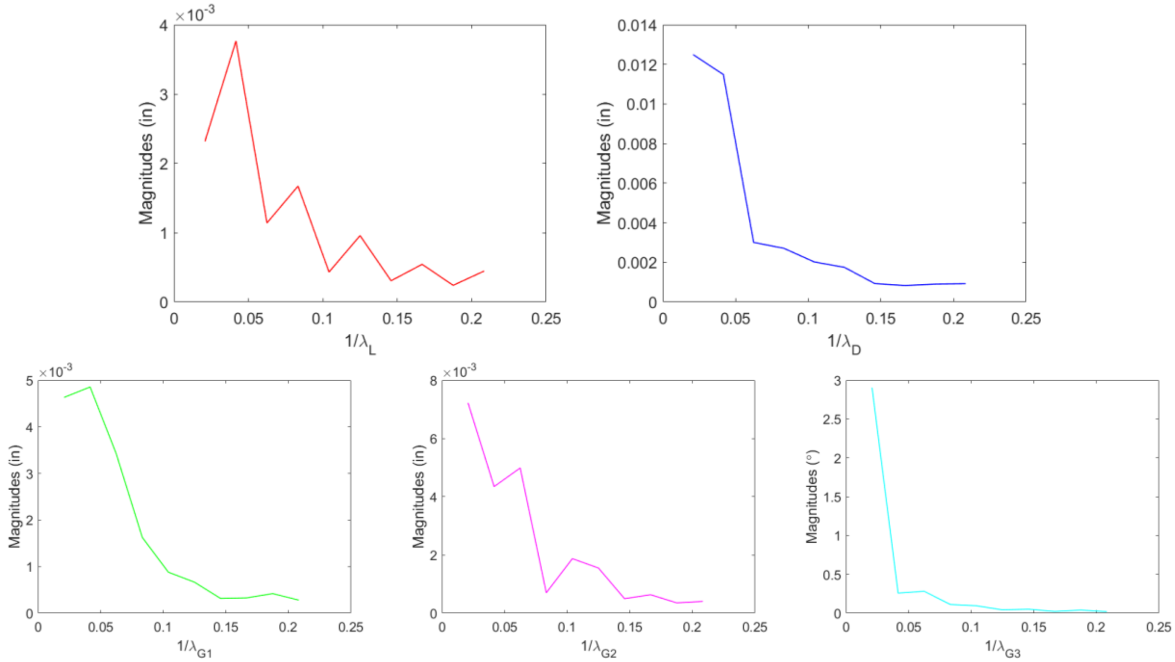

Figure 16 Typical base power spectra of five modal imperfections

Magnitudes from the above base power spectrum are expressed as A_n in Eqs. 4 to 5. In the preliminary study, phases for combinations in a mode imperfection were simplified as zero. Mode 1 to mode 4, i.e., local, distortional, G1, and G2, respectively, use Eq. 4 to combine the modes. Mode 5 should be simulated with a cosine wave from measurement observation, and Eq. 5 is used thereafter. The value of α can be determined simply by summing the multiple waves, as shown in Fig. 17. Simulated imperfections of all of the specimens can be achieved from Eq. 3, where the cross-section deformation mode shapes, ϕ, are known in advance. The imperfections that are obtained are directly added onto the corresponding nodes of the simulated finite-element models.

$$f(y)=\sum_{i=1}^{5}\alpha_i(y)\phi_i(x,z) \tag{3}$$

$$\alpha_i(y)=\sum_{n=0}^{N-1}[A_n \sin(w_n y+\varphi_n)] \tag{4}$$

$$\alpha_i(y)=\sum_{n=0}^{N-1}[A_n \cos(w_n y+\varphi_n)] \tag{5}$$

where
A_n is the magnitude at specific frequency (w_n) from a statistical database;
w_n is the corresponding frequency;
y is the longitudinal position of a simulated member; and
φ_n is a random phase that is distributed uniformly over an interval $[0 \;\; 2\pi]$

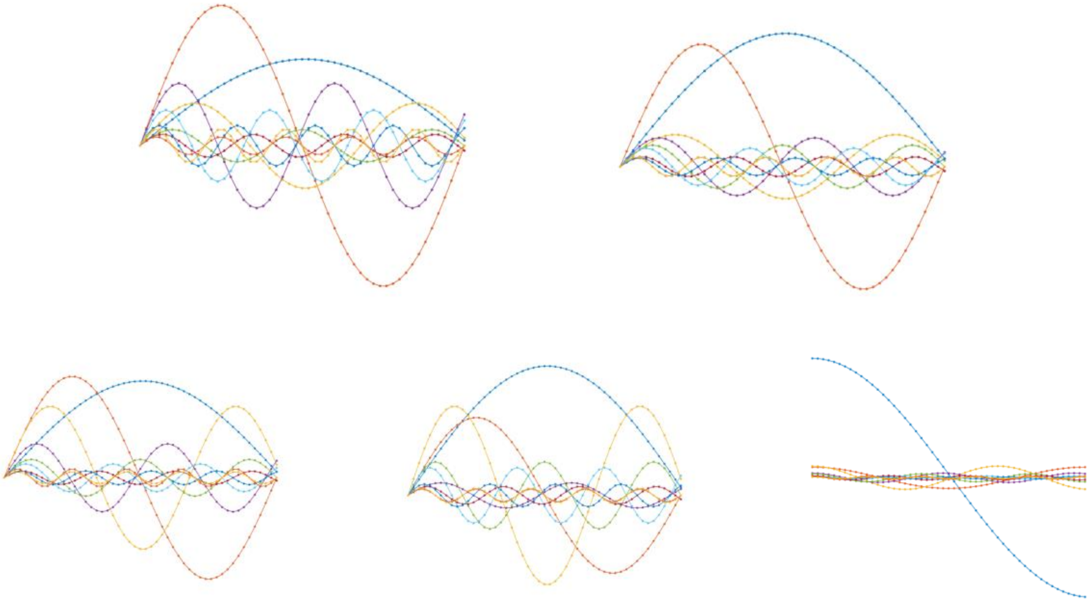

Figure 17 Magnitudes combinations correspond to local, distortional, G1, G2, and G3 imperfections

As nodes with imperfections are obtained, all other procedures to establish a finite element model are similar to the procedures in the previous two sections, such as element definition, material properties, boundary conditions, and analysis method for defining the length of a specific arch. Similar to the traditional approach in the last section, five single mode imperfection simulations have been conducted (Fig. 18). Peak loads are listed in Table 7.

Table 7 Collapse Modeling Results of Traditional Approach

Imperfection mode	**Ultimate Load (kips)**	
	362S162-68	**600S137-54**
Local	9.83	5.16
Distortional	10.08	5.05
Bow	9.98	4.66
Camber	10.39	5.88
Twist	8.63	5.88

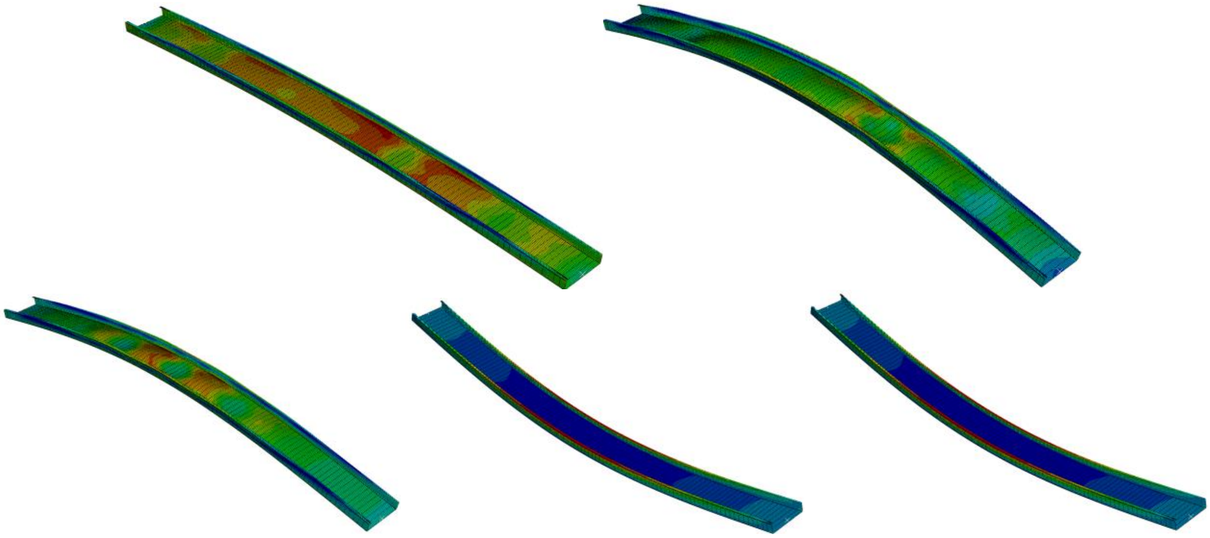

Figure 18 Typical Collapse modeling (600S137-54) of 1D spectral approach: (a) Local; (b) Distortional; (c) Bow; (d) Camber; (e) Twist

5. Discussion

Several comparisons are worth discussing in this paper. A correlation matrix obtained from the true measurement data has been compared with that from the assumption made by Fischer (2016). Fischer assumed correlations among dimensions as follows: (1) two lips are negative correlated with the correlation factor -1; (2) the same-side flanges and lips are negative correlated; and (3) lips are negative correlated with the web height and correlation factors are -0.5, as shown in Table 8.

The true geometry validates Fischer’s first assumption, but it disagrees with the other two assumptions. Same-side flanges and lips are not strongly correlated, but they do have a positive correlation factor. This may be contributed by the strong negative correlation between two flanges due to misalignment of the steel sheet during manufacturing. Web height is not strongly correlated with lip lengths. An interesting phenomenon can be observed im which web height is positively correlated with the left-side lip and negatively correlated with the right-side lip. This further supports the assumption of misalignment of the steel sheet. Moreover, the correlation matrix from true geometry measurement provides an important reference to geometric sensitivities study and structural member quality control.

Table 8 Simulation of correlation matrix (Fisher and Schafer 2016)

ρ	D_1	D_2	B_1	B_2	H
D_1	1.00	-1.00	-1.00	0.00	-0.50
D_2	-1.00	1.00	0.00	-1.00	-0.50
B_1	-1.00	0.00	1.00	0.00	0.00
B_2	0.00	-1.00	0.00	1.00	0.00
H	-0.50	-0.50	0.00	0.00	1.00

The second interesting comparison comes from differences in imperfection characterizations, i.e., conventional imperfection characterization (CIC), modal imperfection decomposition (MID), and 1D spectral method. As observed in Figs. 8 and 9, it is obvious that traditional approaches (CIC and MID) overshoot compared with the actual magnitudes analyzed by the 1D spectral method at the corresponding frequency in cross-section imperfections. As for global imperfections, magnitudes in major components from 1D spectral method resemble to results from traditional approaches. Findings from the study should be further validated with more numerical simulations and compare effects between two approaches.

This comes to the third comparison: single mode imperfections from the traditional approach and 1D spectral modeling. Peak loads are utilized as a major reference. Local imperfections have a difference between traditional and 1D spectral approach are 28.1% and 27% with respect to 362S162-68, and 600S137-54; distortional imperfections are 6.3 and 3.8%, G1 are 3% and 3.12%; G2 are 0.1% and 0.0%; and G3 are 0.1% and 1.25%. These conclusions partially reflect findings from the second comparison in which cross-section imperfections from both methods differ greatly.

6. Conclusions

This paper briefly introduces the full-field laser-based imperfection measurement platform as well as the four-step post-processing toward measurement point clouds from the platform. The first three steps can lead to one application: variation of dimensions and correlation study of cold-formed steel members. The fourth step of post-processing enables another two applications, i.e., imperfection characterizations and finite shell-element analysis. Two traditional-approach characterization, i.e., conventional imperfection characterization and modal imperfection decomposition, and one 1D spectral approach are applied in imperfection studies. It shows that traditional approaches generally are too conservative in estimating imperfections. Reconstructed measurement models are converted into finite shell-element models, the results of which show similar ultimate loads and post-buckling behaviors. True-geometry models can be used as future imperfection modeling validation. Besides, imperfections from two approaches are used for single-mode imperfection numerical simulation. This preliminary study partially shows huge differences existing in two approaches, especially with respect to cross-section imperfections. Future work should apply Monte Carlo simulations to randomly generate the imperfections based on the base power spectrum from 1D spectral representation with reference to true-geometry modeling. An imperfection design protocol will be proposed based on stochastic simulation of geometric imperfections. The proposed design protocol will be validated through experiments in the future work for the use of shell finite element models to characterize the strength of cold-formed steel members and assemblages.

Acknowledgement

This work was partially funded by the National Science Foundation (NSF), Grant 1235196. Any opinions, findings, conclusions, or recommendations stated are those of author(s) and do not necessarily reflect the views of the National Science Foundation.

Reference

ASTM (2015). Load-bearing (transverse and axial) steel studs, runners (tracks), and bracing or bridging for screw application of gypsum panel products and metal plaster bases. **C955-15**.

Fisher, A. W. and B. W. Schafer (2016). Impact of fabrication tolerances on cold-formed stell section properties, stability, and strength. SSRC, Orlando, FL.

Li, Z., M. T. Hanna, S. Adany and B. W. Schafer (2011). "Impact of basis, orthogonalization, and normalization on the constrained Finite Strip Method for stability solutions of open thin-walled members." Thin-Walled Structures **49**(9): 1108-1122.

Zeinoddin, M. V. (2011). Geometric imperfection in cold-formed steel members. Ph.D, Johns Hopkins Unviersity.

Zeinoddini, M. V. (2011). Geometric imperfection in cold-formed steel members. Ph.D, Johns Hopkins Unviersity.

Zeinoddini, V. (2011). Geometric imperfections in cold-formed steel members. Ph. D., Johns Hopkins University.

Zeinoddini, V. M. and B. W. Schafer (2012). "Simulation of geometric imperfections in cold-formed steel members using spectral representation approach." Thin-Walled Structures **60**: 105-117.

Zhao, X. (2016). Measurement and application of geometric imperfections in cold-formed steel members. PhD, Johns Hopkins University.

Zhao, X. and B. W. Schafer (2016). Measured geometric imperfections for Cee, Zee, and Built-up cold-formed steel members. CCFSS, Baltimore.

Zhao, X., M. Tootkaboni and B. W. Schafer (2015). "Development of a Laser-Based Geometric Imperfection Measurement Platform with Application to Cold-Formed Steel Construction." Experimental Mechanics **55**(9): 1779-1790.

Zhao, X., M. Tootkaboni and B. W. Schafer (2016). High fidelity imperfection measurements and characterization for cold-formed steel members. Coupled Instabilities in Metal Structures, Baltimore, MD.